Nanoscale Advances

ROYAL SOCIETY OF CHEMISTRY

PAPER

View Article Online
View Journal | View Issue

Cite this: *Nanoscale Adv.*, 2025, **7**, 6257

Chemical origin of effective functionalization of single atom-MXene catalysts

See-eun Tae,†[a] Zhihao Yen, †[b] Yejin Kim,[a] Mengyuan Zhang,[b] Wenyu Luo,[b] Qingyu Yan, [b] Hyeonseo Jang,[a] Byoung Gun Han,[a] Yeng Ming Lam *[b] and Deok-Yong Cho *[a]

Received 18th May 2025
Accepted 6th August 2025

DOI: 10.1039/d5na00492f

rsc.li/nanoscale-advances

The chemical and atomic structures of Cu-, Ni-, or CuNi-embedded MXene ($Ti_3C_2T_x$, T = O or OH) nanosheet catalysts are examined by using various characterization methods to demonstrate the chemical origin of their composition-dependent evolution. The results of combined X-ray spectroscopy studies and the electrochemical test reveal that Cu ions in (Cu or CuNi):MXene remain active having a +1 valence and form metallic Cu–Cu bonds to enhance the catalytic activity for nitrate reduction. By contrast, Ni ions in (Ni or CuNi):MXene tend to remain bound to O as in $Ni^{2+}O_x$ staying inactive, and, furthermore, hinder the catalytic activity of Cu when co-doped on MXene. It is also demonstrated that chemistry of MXene itself varies by donating electrons from $Ti^{2+/3+}$ to Cu^{2+} to stabilize the active Cu^+ ions. These findings support a combinational mechanism in which both the abundant metallic bonds and the cooperative chemical reconstruction that happened *via* MXene-to-Cu charge transfer facilitate the single atom-aided functionalization of MXene catalysts.

Introduction

MXene nanosheets have attracted wide attention due to their fascinating properties as a support for catalysts owing to their highly hydrophilic surface,[1–4] excellent electrical conductivity,[1,5–9] and tunable surface chemistry[1–3,10–15] together with their environmental friendliness.[16] Extensive studies have shown that by embedding transition metal ions on the surface of MXenes, the functional properties of MXenes can be even further improved and adjusted for numerous applications such as fast energy storage,[5,11,17–21] electrocatalysts[3,16,22–25] and biomedical uses.[26–30] Thus it is highly desirable to find transition metal (TM) species suited for maximizing the catalytic activity.

Improvement of functionality by transition metal (TM) intercalation is correlated with the optimization of electronic and electrochemical properties.[31–34] Among TM atoms, Cu has been often employed for MXene single atom functionalization since Cu:MXene is redox-active and exhibits efficient antibacterial activity,[29] enhanced element adsorption capacity and improved electrocatalytic performance compared to pristine MXenes.[24,30] An alternative option is Ni-embedded MXenes, which also exhibit excellent redox characteristics suitable for HER applications.[21,25]

The detailed mechanism of the catalytic functionalization of TM:MXene is, however, yet to be understood. For instance, Bao *et al.* demonstrated that the catalytic properties of Cu:MXene were associated with the presence of metallic Cu–Cu bonds at the surface,[35] signifying that the abundance of free carriers is essential for catalysis. Meanwhile, Liang *et al.* showed that the TM single atom doping on MXenes can have synergistic effects on urea adsorption by both lowering the adsorption energy and altering the surface structure,[36] implying the structural reconstruction can impact the catalytic activity. It should also be noted that intercalation of TM ions can alter the chemistry of the surface of MXene because TM dopants are in principle chemically active. Thus the functionality of TM:MXene might be provided by intriguing electrochemical and structural evolutions due to TM adhesion. In particular, a combination of Cu and Ni single atom functionalized MXene (CuNi:MXene) is interesting to study, in that a certain interplay between Cu and Ni can take place additionally so as to tune the catalytic activity.

Therefore, it is worth examining the chemical and structural properties of the (Cu, Ni and CuNi)-embedded MXene, to clarify the origin of the catalytic functionalization. Fig. 1 illustrates the schematic of the atomic structure and the relevant electrochemical reactions near the MXene surface ($Ti_3C_2T_x$; where T = –O, –F, or –Cl) with embedded Cu and Ni atoms in CuNi:MXene. This work focused on elucidating the chemical and local structural information of both dopants and MXene itself mainly through the use of synchrotron X-ray absorption spectroscopy (XAS). Soft XAS

[a]*Department of Physics, Jeonbuk National University, Jeonju 54896, Republic of Korea. E-mail: zax@jbnu.ac.kr*

[b]*Department of Materials Science and Engineering, Nanyang Technological University, N4.1-1-28, Nanyang Avenue, Singapore 639798, Singapore. E-mail: ymlam@ntu.edu.sg*

† S.-e. Tae and Z. Yen equally contributed to this work.

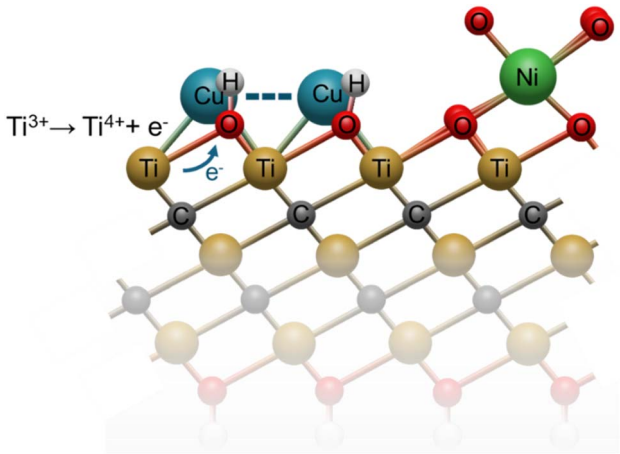

Fig. 1 Schematic for the atomic structure of a MXene nanosheet ($Ti_3C_2T_x$) on which Cu or Ni ions are embedded, to demonstrate the chemical reaction of Ti ions invoked by active Cu ions and the resultant electron transfer to stabilize the Cu^{1+} ionic species.

performed at energies near the edge of each element in (Cu and/or Ni):MXene, *i.e.* Cu, Ni, Ti or O, can reveal the chemical states of the entire specimen, while hard XAS for Cu or Ni can further reveal the coordinated structure of the TM adatoms, *e.g.* Cu–Cu, Ni–O, *etc.* (see Fig. 1 for the atomistic structure).

Experimental details

Materials

Lithium fluoride 300 mesh powder (LiF), methanol (HPLC, ≥99.9% HPLC), hydrochloric acid 37% (HCl), copper(II) chloride dihydrate (ACS reagent, ≥99.0% ($CuCl_2 \cdot 2H_2O$)), nickel(II) nitrate hexahydrate crystals ($(Ni(NO_3)_2 \cdot 6H_2O)$, ACS reagent grade, ≥98%), and sodium borohydride granular ($NaBH_4$) 99.99% trace metal basis were purchased from Sigma-Aldrich, Inc. 200 mesh titanium aluminum carbide MAX phase powder (Ti_3AlC_2) was purchased from ANR Technologies.

Sample preparation

The method for MXene synthesis was adapted and modified from Gogotsi *et al.*[37] The delaminated pristine MXene was synthesized using the single step MILD synthesis method with 12 M LiF and 9 M HCl with a Ti_3AlC_2 MAX phase. Details of the preparation methods of the samples are described in the previous report.[30] As for the Cu/Ni adhesion, the method was adapted and modified from Bao *et al.*[35] $Ti_3C_2T_x$ (250 mg) was sonicated in deionized water (250 mL) for 10 min. 1 mg dL^{-1} of ($CuCl_2$ – 6.7 mL and/or $Ni(NO_3)_2$ – 11.4 mL) solution was added drop-wise into the $Ti_3C_2T_x$ suspension and left to stir for 30 min, followed by sonication for 1 h. The mixture was centrifuged at 10 000 rpm for 30 min and washed with fresh DI water. The obtained products of Cu:MXene, Ni:MXene and CuNi:MXene appeared as black solids.

Measurements

X-ray diffraction (XRD) was performed to identify the crystal structure using a Bruker D8 Advanced instrument equipped with Cu Kα radiation ($\lambda = 1.54$ Å). Surface analysis using X-ray photoelectron spectroscopy (XPS) was conducted with a Kratos AXIS Supra instrument equipped with a monochromatic Al-Kα (1486.6 eV) source. The binding energy (BE) of the XPS spectra was referenced to a C 1s BE of 282.0 eV for Ti–C–Ti in MXene. All the samples were placed in a vacuum overnight at 40 °C before loading into the XPS chamber to clean the surface.

Hard XAS at Cu and Ni K-edges was conducted at the 8C beamline at the Pohang Light Source (PLS) in fluorescence yield mode, whereas soft XAS at the Cu, Ni, and Ti L-edge and O K-edge was done at the 2A beamline at the PLS in total electron yield mode. The (Cu,Ni)–MXene flakes were mounted by gently attaching them on carbon tape and the X-rays were shed perpendicular to the plane of the specimens. All the measurements were done at room temperature. To monitor the homogeneity in the adatoms' distribution, the XAS signals were collected for a few different sample positions. The spectra at different positions were almost identical indicating the uniformity of the adsorbed Cu/Ni atoms within a millimeter scale (limited by the size of the beam).

Electrochemical tests

The electrochemical tests were performed using a typical three-electrode system implemented by an H-type cell in a Solartron electrochemical workstation. The transition metal functionalized MXene was sprayed on a carbon paper and mounted on a stainless steel holder which was used as the working electrode. A Hg/HgO electrode was used as the reference electrode and a platinum mesh (1 cm × 1 cm) was used as the counter electrode. The H-type cell was separated by a Nafion 117 membrane.

For the nitrate reduction reaction (NO_3RR) tests, 30 mL of 1 M KOH + 0.1 M KNO_3 was used as the electrolyte in the cathode compartment while 30 mL of 1 M KOH was used as the electrolyte in the anode compartment. Ar was continuously bubbled in the cathode compartment and magnetic stirring was done at 500 rpm. All the electrodes were referenced against the reversible hydrogen electrode (RHE) using $E_{(V\ vs.\ RHE)} = E_{V\ vs.\ Hg/HgO} + pH \times 0.0591 + 0.0983$. Before all formal testing, 50 cyclic voltammetry (CV) cycles ranging from 0.5 V to −1.0 V with a scan rate of 200 mV s^{-1} were performed in 1 M KOH solution. Linear sweep voltammetry (LSV) was done with a scan rate of 5 mV s^{-1}.

Results and discussion

The crystal structure of the functionalized MXene was characterized by XRD (Fig. 2a) and XPS (Fig. 2b). From Fig. 2a, the absence of signatures for the MAX phase (peaks at a 2θ angle of 9.6°) in the MXene samples' data indicates that the etching and delamination to form MXene were almost completed. The (002) peak of pristine MXene shifted from the MAX phase peak of 9.6° to 6.0°, indicating an expansion of the interlayer spacing due to the successful etching of Al followed by intercalation with Li^+ during the MILD synthesis method. The lattice constants *a* and

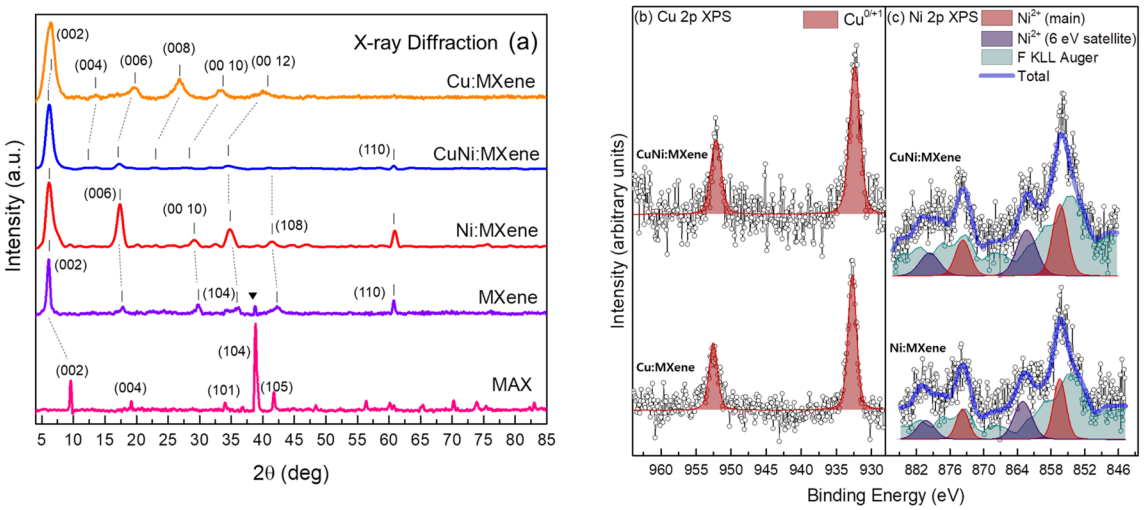

Fig. 2 (a) XRD pattern of the MAX phase (pink), MXene (purple), Cu:MXene (orange), CuNi:MXene (blue), and Ni:MXene (red). The data for the MAX phase and bare MXene are consistent with JCPDS card no. 52-0875 and no. 04-004-2919, respectively. The signatures of MXene and the residual MAX phase were highlighted by vertical short dashes and filled triangles, respectively. (b) Cu 2p and (c) Ni 2p XPS spectra of the MXene samples with fitting curves.

c, estimated from (002) and (110) reflections, are ~3.05 Å and ~29.0 Å, respectively.[38]

The functionalization with Ni on MXene did not introduce any new peaks, indicating no substantial change in the MXene structure except for slight changes in the lattice spacing. The disappearance of the residual peak at 38.9° ((104) reflection in the MAX phase)[39] in the XRD pattern indicates that the MAX phase was separated out completely after functionalization. Meanwhile, after functionalization with Cu, the (002) peak showed a slight upshift to 6.4°, suggesting a decrease in the interlayer spacing by ~2 Å which may originate from deintercalation of Li^+ or loss of bound H_2O molecules driven by the change in MXene's surface charges. It should also be noted that overall XRD patterns changed in the case of Cu doping (Cu:MXene and CuNi:MXene) to be ordered along the *c*-axis with (00*l*) reflections (l = 2 to 12) whilst the in-plane ordering ((110) reflection) appears to be weakened. This implies that the Cu addition might mitigate the lateral atomic ordering within the MXene sheets.

Fig. 2b and c shows the Cu 2p and Ni 2p XPS spectra of the functionalized MXenes, respectively. The Cu 2p spectra consist of a sharp $p_{1/2}$–$p_{3/2}$ doublet separated by a spin orbit splitting energy of 19.8 eV for both samples. The $2p_{3/2}$ BE at ~933 eV indicates that the Cu(0) or Cu(I) valence state was dominant. For CuNi:MXene, however, the features appear broader than those for Cu:MXene, implying inclusion of additional valence states, such as Cu(II). The presence of Cu^{2+} in the CuNi:MXene will be shown in XAS data (Fig. 3a) more clearly.

By contrast, the Ni 2p XPS spectra appear much more complicated. They overlap with F KLL Auger lines severely, and the p doublet with a splitting energy of 17.3 eV further split into two contributions of the main peaks and 6 eV-satellite peaks,[40] which account for an extra energy cost of creating a 3d hole at the valence shell inherent to the Ni atom itself. The results of

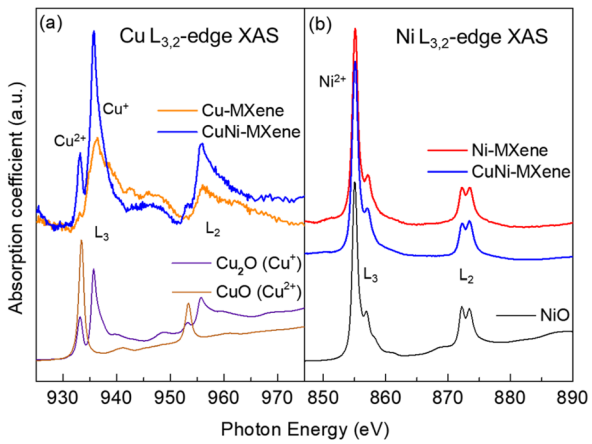

Fig. 3 (a) Cu $L_{3,2}$-edge and (b) Ni $L_{3,2}$-edge soft XAS spectra of the MXene samples together with reference spectra for comparison.

the fitting to the experimental data including all the contributions are displayed in Fig. 2c. It is observed that the intensity ratios of the contributions are roughly preserved irrespective of the samples, signifying an identical chemistry of Ni ions in both samples. The $2p_{3/2}$ BE of the main peak at ~856 eV dictates that the Ni ions are predominantly divalent in both samples.

The atomic concentrations of Cu and Ni in the three functionalized MXene samples were estimated by XPS (see Fig. 2b and c and the survey scans in Fig. S1 in the SI). They were all kept at approximately 0.2 at% with respect to the MXenes regardless of sample or atomic species, as we intended to. Their oxidation states can be confirmed using the O 1s XPS spectra in Fig. S2 in the SI. The contribution of the O–metal bond in the O 1s spectrum (BE = 532–533 eV) was significant for Ni:MXene, less significant for Cu:MXene, and very weak for pristine MXene, which signifies that Ni was prone to oxidation (Ni^{2+}) whereas Cu was significantly less oxidized (Cu^+).

Fig. 3 shows the XAS spectra at the $L_{3,2}$-edges of the adatomic species (namely, Cu and Ni). In Fig. 3a, the XAS spectra of (Cu or CuNi):MXene were compared with the spectra of reference Cu_2O (mainly Cu^+ with partial Cu^{2+} due to surface oxidation)[30] and CuO (mostly Cu^{2+}), in order to estimate the oxidation state of the Cu ions. The photon energies ($h\nu$) of the main peaks (936 eV at the L_3-edge and 956 eV at the L_2-edge) in the spectrum of Cu:MXene coincide with those for Cu_2O, strongly suggesting the predominance of Cu^+.[30] The dominant contribution of Cu^+ can also be confirmed using the Cu K-edge XAS spectrum in Fig. S3 in the SI. The X-ray absorption near edge structure (XANES) and its $h\nu$ derivative (Fig. S3a and b, respectively) clearly show that the $h\nu$ of the highest slope of the pre-edge peak is approximately 8981 eV, which is for Cu^+.[31] These results were consistent with the findings in the XPS studies shown in Fig. 2b and in ref. 20, 36 and 41.

Meanwhile, the chemical state of Cu in CuNi:MXene appears different from that in Cu:MXene. It is shown in the spectrum in Fig. 3a that sharp peaks emerge at 933 eV (L_3) and 953 eV (L_2), being consistent with the presence of Cu^{2+} (as in the case of CuO). Therefore, it can be said that Cu ions in CuNi:MXene were more oxidized than those in Cu:MXene. This signifies that the presence of Ni can expedite the oxidation of Cu ($Cu^{1+} \rightarrow Cu^{2+} + e$), consistent with the result from the XPS analysis.

On the other hand, the Ni ions appear to have robust Ni^{2+} oxidation states in both samples. Fig. 3b shows the Ni $L_{3,2}$-edge spectra of the Ni:MXene and CuNi:MXene samples together with the spectrum of reference NiO (Ni^{2+}). All three spectra are almost identical indicating the predominance of Ni^{2+} in the MXene samples. The predominance of Ni^{2+} is also confirmed by Ni K-edge XANES analysis in Fig. S3c and d.

Moreover, we can infer that the Ni ions were likely coordinated by oxygen ions octahedrally like in NiO.[42] The L-edge spectrum of Ni^{2+} ions (with eight d electrons, *i.e.* two holes) is well known to be very sensitive to the electronic configuration interaction and the (anion-to-cation) charge transfer effect so that the resemblance in the Ni L-edge spectra can even resolve the atomic species of anions and their local coordination geometry.[42,43] Fig. S4 in the SI shows the O K-edge XAS spectra, which reflect the unoccupied electronic structure of the cations that were indeed bound with O atoms only. Although most of the features were dominated by the features from MXene itself, a systematic increase in the Ni–O feature at $h\nu \sim 532$ eV (with an increasing Ni/Cu ratio) was clearly observed. This suggests that Ni was indeed bound with O. In contrast, the features of Cu–O do not appear prominent, implying that Cu–O bonds might not be as strong as Ni–O bonds. This tendency is very consistent with the O 1s XPS data (Fig. S2).

Therefore, it is conclusive that Ni ions in both Ni:MXene and CuNi:MXene were oxidized to become NiO_x indeed bound with surrounding O ions, which presumably originate from the MXene itself (see Fig. 1). These O ions may influence the chemistry of nearby ions such as Cu or Ti (in MXene). For instance, the chemical state of the Cu ions may in part remain in a high valence (+2) state since the surrounding O may suppress the electron donation from MXene as depicted in Fig. 1. Thereby the Cu and Ni co-adhesion might result in a partially higher valence (Cu^{2+}) compared to the case of Cu adhesion on MXene (predominantly Cu^+) (see Fig. 3a).

As such, it is shown that degrees of oxidation of the inserted TM ions vary depending on the atomic species; Cu on MXene mainly remains as Cu^+ (aside from Cu^{2+} in CuNi:MXene), whereas Ni on MXene is fully oxidized into a Ni^{2+} state. It should be noted that the precursors used in the synthesis readily have +2 valences so that if physically adsorbed, the TM ions should have preferred +2 valences. Therefore, the chemical adhesion of Cu^+ necessitates an extra reduction process ($Cu^{2+} \rightarrow Cu^+$) for taking additional electrons presumably from MXene. The reduction capability of MXene was recently observed by Xiao *et al.*,[44] very consistent with the abundance of (relatively reduced) Cu^+ ions.

Therefore, the stabilization of Cu^+ on MXene instead of Cu^{2+} should accompany an electron transfer from MXene. An additional oxidation of MXene itself was indeed observed in Ti L-edge XAS. Fig. 4 shows the Ti $L_{2,3}$-edge XAS spectra of the three MXene samples together with those from pristine MXene (taken from ref. 32) and TiO_2 (Ti^{4+}) as references. In the pristine MXene ($Ti_3C_2T_x$, T = –O or –OH), Ti is originally di- or tri-valent.[30] In the case of Ni:MXene, the spectrum appears very similar to that of the pristine MXene indicating that the chemistry of Ti ions in MXene remains mostly unchanged. It suggests that the MXene remains inactive during the Ni^{2+} adhesion. On the other hand, the Ti spectrum of Cu:MXene suffers from a significant evolution being similar to that of TiO_2 (Ti^{4+}), clearly showing an additional oxidation of Ti in MXene.

The resultant Ti oxidation and electron donation to the Cu site are described in Fig. 1. From the previous discussion, it is reasonable to interpret that the Ti oxidation is essential for stabilizing the Cu^+ valence. Nevertheless, the overall similarity in line shape of Cu:MXene to TiO_2 was rather surprising

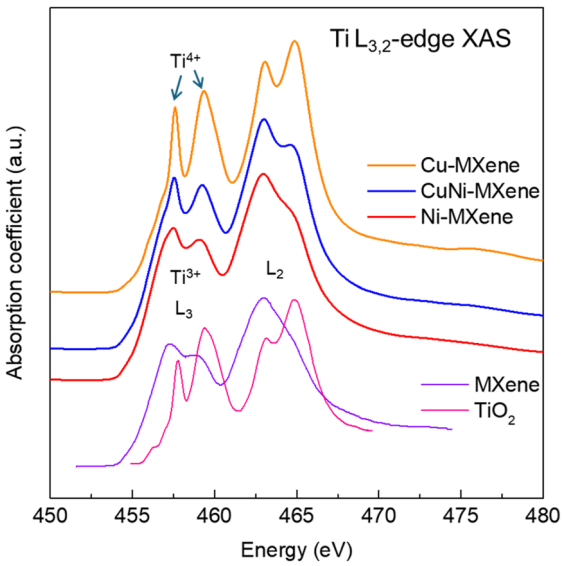

Fig. 4 Ti $L_{3,2}$-edge XAS spectra of the (Cu or Ni):MXene samples showing an evolution of Ti oxidation in accordance with the Cu incorporation. The spectra of pristine MXene and TiO_2 are appended for comparison.

because it infers that the additional Ti oxidation occurred extensively or at least within the probing depth of soft XAS (~5 nm); hence this is not being confined to only the surface. Interestingly, the spectral evolution appears systematic upon increasing the Cu/Ni ratio; the spectrum of CuNi:MXene shows a similar trend (of Ti oxidation) but the tendency is not as clear as in Cu:MXene, implying a lower degree of Ti oxidation than in the case of Cu:MXene. This aligns with the incomplete $Cu^{2+} \rightarrow Cu^{+}$ reduction in CuNi:MXene as seen in the Cu L-edge XAS spectrum (see Fig. 3a), in that the electrons needed for the adatoms' reduction cannot be supported elsewhere but from the MXene.

In order to study the local bonding environment of the Cu and Ni adatoms, the Fourier-transformed (FT) extended X-ray absorption fine structure (EXAFS) analysis was conducted. Fig. 5 shows the (a) Cu K-edge and (b) Ni K-edge FT EXAFS spectra of the specimens. For comparison, the spectra from the reference Cu foil (Cu^0) and Ni foil (Ni^0) are appended in the figure. The FT was processed for the electron wavenumber (k) range of k = 2–10 $Å^{-1}$ for k^2-weighted XAFS oscillations using ATHENA.[45] The peaks are assigned according to the reduced radial distance, R, as either Cu–O or Ni–O (for $R \sim 1.6$ Å), Cu–Cu/Ti or Ni–Ni (for $R \sim 2.3$ Å), *etc.* The shortest R features, *i.e.* $R \sim 1.6$ Å, should be related mainly to the –O direct bond, whose presence was confirmed by O K-edge XAS (Fig. S4).

The Cu K-edge EXAFS data of the MXene samples (Fig. 5a) show rather broad features including Cu–O, Cu–Cu/Ti and multiple scatterings or indirect bonds over a wide range (1–3 Å), whereas the Ni K-edge EXAFS data of the MXene samples (Fig. 5b) show sharp features for Ni–O only with a very weak feature in the higher R range. This evidently shows that the Cu adatoms have cation-to-cation metallic bonds whereas the Ni adatoms do not. It is noteworthy that in CuNi:MXene, there exists Cu–metal (Cu, Ni or Ti) bonds whilst there is only a very weak signature of Ni–metal bonds (probably for Ni–Ti). Thus, it is evident that there are no Cu–Ni bonds. Then the signature of the Cu–metal bonds should originate either from Cu–Cu bonds among some aggregated Cu clusters or from Cu–Ti bonds representing chemisorption onto the MXene support. By contrast, the Ni adatoms are far from one another due to preferential bonding to intervening O-ions, as is evidenced by the strong Ni–O bonds in Fig. 3b and 5b.

Fig. 5c and d shows the results of the wavelet transformation (WT) of the CuNi:MXene's EXAFS data processed by using a Morlet wavelet[46] with κ = 10 Å and σ = 1 $Å^{-1}$ for the k^2-weighted EXAFS. By comparing the high magnitude positions in R–k space with the reference films' data, the origins of the EXAFS features shown in Fig. 5a and b can be further clarified. The high magnitude regions can be identified as Cu–T (T = O) or Cu–(Cu or Ti) as shown in Fig. 5c and as Ni–T (T = O) or Ni–Ti as shown in Fig. 5d in accordance with the R values (vertical axes). The WT EXAFS data for Cu foil and Ni foil are displayed in Fig. S5 in the SI. They show that Cu–Cu and Ni–Ni signatures (if exist) appear in the coordinate near (k, R) ~ (7 $Å^{-1}$, 4 Å). The feature for Cu–Cu was indeed observed as is highlighted by an asterisk in Fig. 5c, whereas no noticeable feature for Ni–Ni exists in Fig. 5d. This conclusively shows that only Cu–Cu bonds may exist on the surface of TM-embedded MXene.

The results of the EXAFS fitting are displayed in Fig. S6 and Table S1 in the SI. A two-shell (Cu–O and Cu–Cu) model for Cu and a single shell (Ni–O) model for Ni were employed to fit the EXAFS in the R = 1–3 Å range. The estimated phase (Δ)-corrected atomic distances ($R + \Delta$) for Cu–O and Ni–O were in the range of 2.01–2.04 Å, which is reasonable for many 3d transition metal oxides. Meanwhile, $R + \Delta$ for Cu–Cu was in the range of 2.41–2.43 Å, which is smaller than the shortest Cu–Cu bond length (~2.54 Å) in a face-centered-cubic Cu metal. This reflects a significant contraction in ionic radii of Cu^+ ($3d^{10}$; no 4s electron) compared to Cu^0 ($3d^{10}4s^1$). Therefore, the structural information also supports that the Cu^+ is the dominant ionic species in Cu-embedded MXene.

To correlate the chemical and structural evolution by TM addition with the catalytic activity, the NO_3RR measurement[47] was conducted for the 3 functionalized MXene samples. Fig. 6

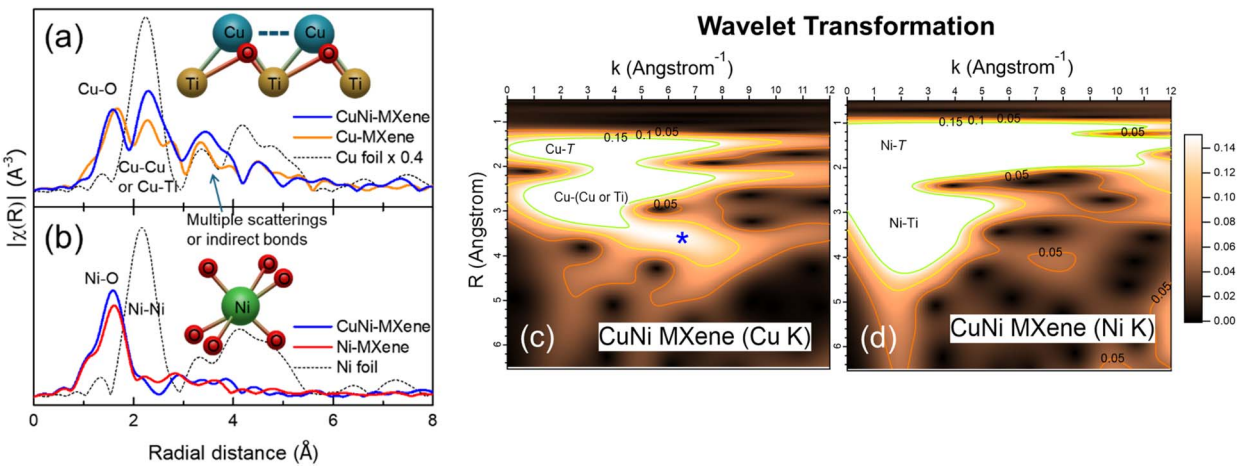

Fig. 5 (a) Cu K-edge and (b) Ni K-edge FT EXAFS spectra of the MXene samples together with reference spectra for comparison. The WT maps of the Cu K-edge and Ni K-edge XAFS for the CuNi:MXene sample are appended as (c) and (d), respectively.

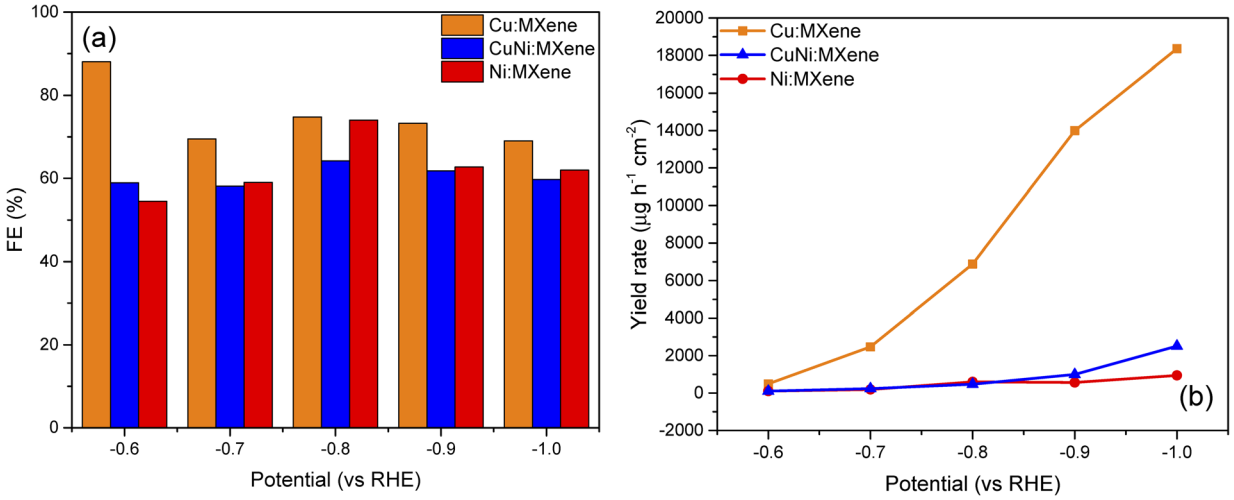

Fig. 6 (a) Faradaic efficiency (FE) and (b) the yield rate of the NO_3 reduction reaction of Cu:MXene (orange), CuNi:MXene (blue) and Ni:MXene (red).

shows (a) the faradaic efficiencies (FEs) and (b) the yield rates of the samples loaded on the working electrode, whose values can be determined using equations introduced in Section 1 in the SI (see Fig. S7 in the SI for the LSV data). Fig. 6a shows that the functionalized MXenes exhibit good efficiencies for the NO_3RR in general. It is noteworthy that Cu:MXene exhibits overall high FEs compared to the other two samples, particularly at a potential of −0.6 V (88%). At this potential, however, the yield rate is too low to be used for the NO_3RR (see Fig. 6b). The yield rate increases rapidly with the decreasing value of the potential (rightward in Fig. 6b) reaching over 18 000 μg h^{-1} cm^{-2} at −1.0 V.

Meanwhile, Ni:MXene or CuNi:MXene exhibits FEs comparable to those of Cu:MXene (Fig. 6a), but have much lower yield rates than the case of Cu:MXene (Fig. 6b), indicating inferior NO_3RR activity. Also, the yield rate of CuNi:MXene was slightly higher than that of Ni:MXene. Thus, we can tell that Cu addition is the key to enhance the NO_3RR activity of MXene, which implies that the catalytic functionality can be attributed overall to the adatom's genuine properties. A high density of the delocalized electrons around the Cu–Cu bonds or the prevalence of Cu^+ (over Cu^{2+}; Fig. 3), that was stabilized *via* electron donation from the MXene support (Fig. 4), can contribute to the improvement in the yield rate (Fig. 6b).

On the other hand, as seen in Fig. 5a, Cu:MXene and CuNi:MXene have similar magnitudes of the Cu–Cu (or Ti) bond peaks ($R + \Delta \sim 2.4$ Å) to each other, suggesting similar concentrations of the metallic bonds irrespective of the presence of Ni. However, the yield rate of CuNi:MXene was much closer to that of Ni:MXene rather than that of Cu:MXene (Fig. 6b), signifying that Ni atoms in NiO_x forming at the surface are not only inactive by themselves but also hinder the functionality of the embedded Cu atoms. Since the atomic concentrations of Cu were approximately 0.2 at% for both Cu:MXene and CuNi:MXene, the inferior yield rate in the presence of $Ni(O_x)$ (Fig. 3b) cannot be associated with the abundance of the metallic bonds. Instead, the hindrance effect of Ni–O clusters can be related to the blocking of the electron transfer from MXene to Cu needed for stabilizing reduced Cu ions (Cu^+), which in turn leaves fully oxidized Cu ions (Cu^{2+}) in part (as shown in Fig. 3a). Therefore, the distribution of the active (Cu) and inactive ($Ni(O_x)$) adatoms is also important in determining the catalytic functionality of the TM:MXene.

Conclusions

In conclusion, combinatorial chemical and structural analyses (XRD, XPS and soft/hard XAS) together with an electrochemical test (NO_3RR) on (Cu, Ni, or CuNi)-embedded MXene revealed the detailed chemical interactions at the functionalized MXene surface and their roles in catalytic functionalization: active (reduced) Cu^+ ions which tend to form metallic bonds, inactive Ni^{2+} (with NiO_x clusters) which can hinder the catalytic activity associated with Cu, and electron-donating (oxidized) Ti^{4+} from MXene to stabilize the Cu^+ species. These findings clarify the electrochemical mechanism of single atom catalysts with a MXene support, in which not only the abundance of delocalized electrons (metallicity) but also the cooperative MXene-single atom chemical reconstruction contribute to the catalytic functionalization of the MXene surface.

Author contributions

S.-e. T., Z. Y., Y. M. L. and D.-Y. C. designed the study. Y. K., H. J., B. G. H. and D.-Y. C. conducted the synchrotron measurement and interpreted the data. Z. Y., M. Z., W. L., and Q. Y. fabricated the samples, performed XRD and XPS, and measured the NO_3RR activity. Y. M. L. and D.-Y. C. supervised the study. The manuscript was prepared by S.-e. T., Z. Y., Y. M. L and D.-Y. C., and all the authors approved the final version of the manuscript.

Conflicts of interest

There are no conflicts to declare.

Data availability

The data supporting this article have been included as part of the SI.

Quantification of ammonia, calculation methods for faradaic efficiency and yield rate, XPS survey and O 1s spectra, Cu/Ni K-edge XANES spectra, O K-edge XAS spectra, wavelet-transformed EXAFS data, EXAFS fitting results, and LSV data. See DOI: **https://doi.org/10.1039/d5na00492f**.

Acknowledgements

This work was supported by the Ministry of Education, Singapore, MOE Tier 1 (RG8/22) and by the National Research Foundation funded by the Ministry of Science and ICT of Korea (2021R1A2C1004644). The authors would like to acknowledge the Facility for Analysis, Characterization, Testing, and Simulation (FACTS), Nanyang Technological University, for use of their X-ray facilities.

References

1 B. Anasori, M. R. Lukatskaya and Y. Gogotsi, *Nat. Rev. Mater.*, 2017, **2**, 16098.
2 H. Lin, Y. Chen and J. Shi, *Adv. Sci.*, 2018, **5**, 1800518.
3 H. Wang and J. M. Lee, *J. Mater. Chem. A*, 2020, **8**, 10604–10624.
4 M.-Q. Zhao, C. E. Ren, Z. Ling, M. R. Lukatskaya, C. Zhang, K. L. Van Aken, M. W. Barsoum and Y. Gogotsi, *Adv. Mater.*, 2015, **27**(2), 339–345.
5 M. Ghidiu, M. R. Lukatskaya, M.-Q. Zhao, Y. Gogotsi and M. W. Barsoum, *Nature*, 2014, **516**(7529), 78–81.
6 M. R. Lukatskaya, S. Kota, Z. Lin, M.-Q. Zhao, N. Shpigel, M. D. Levi, J. Halim, P.-L. Taberna, M. W. Barsoum, P. Simon and Y. Gogotsi, *Nat. Energy*, 2017, **2**(8), 17105.
7 C. Zhang, M. Beidaghi, M. Naguib, M. Lukatskaya, M.-Q. Zhao, B. Dyatkin, K. M. Cook, S. J. Kim, B. Eng, X. Xiao, D. Long, W. Qiao, B. Dunn and Y. Gogotsi, *Chem. Mater.*, 2016, **28**(11), 3937–4043.
8 F. Shahzad, M. Alhabeb, C. B. Hatter, B. Anasori, S. M. Hong, C. M. Koo and Y. Gogotsi, *Science*, 2016, **353**(6304), 1137–1140.
9 A. Sarycheva, A. Polemi, Y. Liu, K. Danadekar, B. Anasori and Y. Gogotsi, *Sci. Adv.*, 2018, **4**, 9.
10 Y. Gogotsi and B. Anasori, *ACS Nano*, 2019, **13**, 8491–8494.
11 Q. Jiang, Y. Lei, H. Liang, K. Xi, C. Xia and H. N. Alshareef, *Energy Storage Mater.*, 2020, **27**, 78–95.
12 J. Halim, M. R. Lukatskaya, K. M. Cook, J. Lu, C. R. Smith, L.-Å. Näslund, S. J. May, L. Hultman, Y. Gogotsi, P. Eklund and M. W. Barsoum, *Chem. Mater.*, 2014, **26**(7), 2374–2381.
13 Y. Dall'Agnese, M. R. Lukatskaya, K. M. Cook, P. L. Taberna, Y. Gogotsi and P. Simon, *Electrochem. Commun.*, 2014, **48**, 118–122.
14 O. Mashtalir, M. R. Lukatskaya, A. I. Kolesnikov, E. Raymundo-Piñero, M. Naguib, M. W. Barsoum and Y. Gogotsi, *Nanoscale*, 2016, **8**(17), 9128–9133.
15 Z. W. Seh, K. D. Fredrickson, B. Anasori, J. Kibsgaard, A. L. Strickler, M. R. Lukatskaya, Y. Gogotsi, T. F. Jaramillo and A. Vojvodic, *ACS Energy Lett.*, 2016, **1**(3), 589–594.
16 Y. Zhang, L. Wang, N. Zhang and Z. Zhou, *RSC Adv.*, 2018, **8**, 19895–19905.
17 G. Zou, Z. Zhang, J. Guo, B. Liu, Q. Zhang, C. Fernandez and Q. Peng, *ACS Appl. Mater. Interfaces*, 2016, **8**, 22280–22286.
18 M. R. Lukatskaya, O. Mashtalir, C. E. Ren, Y. Dall'Agnese, P. Rozier, P. L. Taberna, M. Naguib, P. Simon, M. W. Barsoum and Y. Gogotsi, *Science*, 2013, **341**(6153), 1502–1505.
19 M. D. Levi, M. R. Lukatskaya, S. Sigalov, M. Beidaghi, N. Shpigel, L. Daikhin, D. Aurbach, M. W. Barsoum and Y. Gogotsi, *Adv. Energy Mater.*, 2015, **5**(1), 1400815.
20 Y. Zhang, Z. Guo, J. Zhou and D. Sun, *Ceram. Int.*, 2022, **48**, 30524–30535.
21 O. P. Nanda, A. G. Prince, L. Durai and S. Badhulika, *Energy Fuels*, 2023, **37**, 4701–4710.
22 P. Kumar, S. Singh, S. A. R. Hashmi and K. H. Kim, *Nano Energy*, 2021, **85**, 105989.
23 J. Zhang, Y. Zhao, X. Guo, C. Chen, C.-L. Dong, R.-S. Liu, C.-P. Han, Y. Li, Y. Gogotsi and G. Wang, *Nat. Catal.*, 2018, **1**(12), 985–992.
24 L. Liu, Q. Zhao, R. Liu and L. Zhu, *Appl. Catal., B*, 2019, **252**, 198–204.
25 K. Gothandapani, G. T. Selvi, R. S. Jennifer, V. Velmurugan, S. Pandiaraj, M. Muthuramamoorthy, S. Pitchaimuthu, V. Raghavan, A. C. J. Malathi, A. Alodhayb and A. N. Grace, *Int. J. Hydrogen Energy*, 2024, **52**, 1164–1171.
26 A. Szuplewska, D. Kulpińska, A. Dybko, M. Chudy, A. M. Jastrzębska, A. Olszyna and Z. Brzózka, *Trends Biotechnol.*, 2020, **38**, 264–279.
27 M. Soleymaniha, M. A. Shahbazi, A. R. Rafieerad, A. Maleki and A. Amiri, *Adv. Healthcare Mater.*, 2019, **8**(1), 1801137.
28 A. Zamhuri, G. P. Lim, N. L. Ma, K. S. Tee and C. F. Soon, *Biomed. Eng. Online*, 2021, **20**(1), 33.
29 N. Talreja, M. Ashfaq, D. Chauhan and R. V. Mangalaraja, *Mater. Chem. Phys.*, 2023, **294**, 127029.
30 Z. Yen, T. Salim, C. Boothroyd, P. F. Haywood, C.-T. Kuo, S.-J. Lee, J.-S. Lee, D.-Y. Cho and Y. M. Lam, *ACS Appl. Nano Mater.*, 2023, **6**, 16486–16496.
31 S. Wee, X. Lian, E. Vorobyeva, A. Tayal, V. Roddatis, F. L. Mattina, D. G. Vazquez, N. Shpigel, M. Salanne and M. R. Lukatskaya, *ACS Nano*, 2024, **18**(14), 10124–10132.
32 A. Al-Temimy, K. Prenger, R. Golnak, M. Lounasvuori, M. Naguib and T. Petit, *ACS Appl. Mater. Interfaces*, 2020, **12**, 15087–15094.
33 A. Al-Temimy, F. Kronast, M. A. Mawass, K. A. Mazzio, K. Prenger, M. Naguib, T. Petit and S. Raoux, *Appl. Surf. Sci.*, 2020, **530**, 147157.
34 S. Adil and J.-O. Kim, *Sep. Purif. Technol.*, 2023, **326**, 124725.
35 H. Bao, Y. Qiu, X. Peng, J.-A. Wang, Y. Mi, S. Zhao, X. Liu, Y. Liu, R. Cao, L. Zhuo, J. Ren, J. Sun, J. Luo and X. Sun, *Nat. Commun.*, 2021, **12**, 238.

36 C. Liang, Z. Yen, T. Salim and Y. M. Lam, *Phys. Chem. Chem. Phys.*, 2023, **25**, 31874.
37 M. Alhabeb, K. Maleski, B. Anasori, P. Lelyukh, L. Clark, S. Sin and Y. Gogotsi, *Chem. Mater.*, 2017, **29**, 7633–7644.
38 X. Mu, D. Wang, F. Du, G. Chen, C. Wang, Y. Wei, Y. Gogotsi, Y. Gao and Y. Dall'Agnese, *Adv. Funct. Mater.*, 2019, **29**, 1902953.
39 H. Fang, Y. Pan, M. Yin and C. Pan, *J. Mater. Sci.: Mater. Electron.*, 2019, **30**, 14954–14966.
40 S. Hüfner and G. K. Wertheim, *Phys. Lett. A*, 1975, **51**, 299–300.
41 B. Wang, Q. Shu, H. Chen, X. Xing, Q. Wu and L. Zhang, *Metals*, 2022, **12**, 2022.
42 M. W. Haverkort, S. I. Csiszar, Z. Hu, S. Altieri, Z. Tanaka, H. H. Hsieh, H.-J. Lin, C. T. Chen, T. Hibma and L. H. Tjeng, *Phys. Rev. B: Condens. Matter Mater. Phys.*, 2004, **69**, 020408.
43 D.-Y. Cho, S.-J. Song, U. K. Kim, K. M. Kim, H. K. Lee and C. S. Hwang, *J. Mater. Chem. C*, 2013, **1**, 4334–4338.
44 Y. Xiao, C. Men, B. Chu, Z. Qin, H. Ji, J. Chen and T. Su, *Chem. Eng. J.*, 2022, **446**, 137028.
45 B. Ravel and M. Newville, *J. Synchrotron Radiat.*, 2005, **12**, 537–541.
46 H. Funke, A. C. Scheinost and M. Chukalina, *Phys. Rev. B: Condens. Matter Mater. Phys.*, 2005, **71**, 094110.
47 W.-D. Zhang, H. Dong, L. Zhou, H. Wu, H.-R. Wang, X. Yan, Y. Jiang, J. Zhang and Z.-G. Gu, *Appl. Catal., B*, 2022, **317**, 121750.